

OPEN

From Point to Filament Defects in Hybrid Nematic Films

Cesare Chiccoli¹, Paolo Pasini¹, Claudio Zannoni^{2*}, Gregor Skačej³, Hiroyuki Yoshida^{4,5}, Taiga Hiroshima⁴, Kanta Sunami⁴, Tomohiro Ouchi⁴ & Masanori Ozaki⁴

We have studied nematic hybrid films with homeotropic alignment at the top surface and various controlled degrees of in plane ordering, going from a random degenerate organization to a completely uniform alignment along one direction, at the bottom one. We show, by Monte Carlo (MC) computer simulations and experiments on photopatterned films with the bottom support surface fabricated with in-plane order similar to the simulated ones, that the point defects observed in the case of random planar orientations at the bottom tend to arrange along a filament as the surface ordering is sufficiently increased. MC simulations complement the polarized microscopy texture observations allowing to inspect the 3D structure of the defects and examine the role of elastic constants.

Contrary to what the name would suggest, defects are not necessarily a negative feature of materials. Indeed “defect engineering” is a blooming methodology for fabricating novel complex molecular organizations starting from liquid crystal topological defects^{1–15}. In essence, the approach is normally based on the fact that defects correspond to high free energy regions of the system, which makes them prone to be attacked by suitable reagents or, in turn, capable of attracting colloidal or nano-particles in an effort to reduce the local free energy excess.

The methodology has been employed, e.g. to prepare ordered arrays of gold or other metal nanoparticles with the goal to prepare self-assembling metamaterials⁴ and even active bacterial system¹⁶. Defects in liquid crystals correspond to well defined categories endowed with a certain topological charge s ^{17,18}, and their positions and nature can, to some extent, be controlled from outside, employing suitable boundary conditions and external fields. For instance in a thin film of nematic spread on a spherical colloidal particle, where the total topological charge should be 2, four $s = 1/2$ defects placed in a tetrahedral arrangement appear, making the particle a kind of tetravalent “colloidal atom”². This valence can, however, be changed by the application of suitable multipolar fields³ while the defect location can be changed, e.g. varying the shape of the colloidal core from spherical to ellipsoidal¹⁹. In thin nematic films, sandwiched between two flat surfaces with a null total topological charge ($s = 0$), the occurrence and nature of defects can also be controlled by imposing, apart from external fields, various types of boundary conditions with the help of appropriate surface anchoring agents. Thus, defects should be absent in a flat cell with a uniform alignment either parallel to a certain direction of the surface, \mathbf{r} , or tilted with respect to it, realizing a monodomain. More generally, when the film is so thin that the director can be considered to live in two dimensions (2D), homotopy theory shows that there can be in principle infinitely many types of disclinations in director orientations classified by their semi-integer or integer topological charge s ^{20–22}. These various defects have of course different free energy and in practice only the ones with smallest s are normally observed. The situation is different in the bulk, where only half integer defects are allowed, while integer ones can be eliminated and relax out, e.g. by the escape in the third dimension mechanism²³.

In the present work, we are interested in nematic films with hybrid boundary conditions, where the liquid crystal has planar degenerate anchoring at the solid support surface and homeotropic alignment at the top interface, defects will appear when the film thickness h is much smaller than the lateral size L ²⁴. This kind of stable defects for hybrid systems has been investigated experimentally and on the basis of continuum theory (see for example²⁵) as well as by lattice spin simulations²⁴. In particular, we have shown in the past that Monte Carlo computer simulations of lattice spin models with nearest neighbor interactions like the Lebwohl-Lasher^{26,27} one, where only particle orientations are considered, can reproduce the appearance of stable point defects in hybrid nematic films²⁴. In practice these contrasting boundary conditions are implemented in the simulations with two

¹INFN Sezione di Bologna, Via Irnerio 46, 40126, Bologna, Italy. ²Dipartimento di Chimica Industriale Toso Montanari, Università di Bologna and INSTM, Viale Risorgimento 4, I-40136, Bologna, Italy. ³Faculty of Mathematics and Physics, University of Ljubljana, Jadranska 19, SI-1000, Ljubljana, Slovenia. ⁴Division of Electrical, Electronic and Informational Engineering, Osaka University, 2-1 Yamada-oka, Suita-shi, Osaka-fu, 565-0871, Japan. ⁵JST, PRESTO, 4-1-8 Honcho, Kawaguchi, Saitama, 332-0012, Japan. *email: Claudio.Zannoni@unibo.it

additional, static, layers of spins where those at the bottom ($z=0$) have random fixed orientations in the horizontal (x, y) plane, while those of the top ($z=h$) layer are fixed along the surface normal²⁴. It has also been reported that disclination lines can be formed in a hybrid nematic cell where the two facing flat surfaces enclosing the nematic are respectively treated to induce an orientation perpendicular to the surface at the top ($z=h$), as in the previous case, and an homogeneous, uniform, in plane alignment along x or y at $z=0$ ²⁸. However, the surface order needs not to be complete and, more generally, the extent of ordering at the surface can be quantified introducing a two dimensional surface order parameter $\langle T_2 \rangle$ ²⁹,

$$\langle T_2 \rangle = \langle \cos(2\alpha) \rangle, \quad (1)$$

where α is the orientation of a molecule belonging to the surface plane with respect to the global easy axis of the surface. The two limiting situations just described correspond to $\langle T_2 \rangle = 0$ (planar degenerate) or 1 (perfect alignment along one direction in the plane). The effect on the molecular organization inside a nematic film in this intermediate situation with only partial surface order is not obvious, particularly for what concerns the type of defects formed. As an example, it is not known, as far as we are aware, if there is some critical surface order that enforces the transition from points to lines or walls, everything else being the same, or actually which type of defects occurs.

Clarifying the way in which specific defect organizations can be created is clearly important, also in view of the aforementioned applications, and in the present paper we wish to study how the point defects transform by changing the bottom surface of the hybrid film from a random planar molecular orientations to a fully ordered one by gradually increasing the percentage of ordering. We tackled the problem both by Monte Carlo computer simulations and real experiments. Simulations allow to precisely define the surface order and to provide input for preparing similarly ordered support surfaces by photofabrication techniques (see, e.g.¹⁴).

The Simulation Model

We have chosen to model our hybrid thin films adapting the Gruhn-Hess-Luckhurst-Romano (GHLR) model³⁰⁻³² which consists of a system of interacting centers ("spins") placed at the sites of a regular lattice. The total Hamiltonian U_N is written as follows:

$$U_N = \frac{1}{2} \sum_{\substack{i,j \in \mathcal{F}, \\ i \neq j}} U_{ij} + J \sum_{\substack{i \in \mathcal{F}, \\ j \in \mathcal{S}}} U_{ij}, \quad (2)$$

where \mathcal{F}, \mathcal{S} are the set of particles in the bulk and at the surfaces, respectively, and the parameter J corresponds to the strength of the coupling of the sample spins with the surface boundary spins (here we assume $J=0.5$). The particles interact through the second rank nearest neighbour attractive pair pseudo-potential³²:

$$U_{ij} = \varepsilon_{ij} \left\{ \lambda [P_2(\mathbf{u}_i \cdot \mathbf{s}_{ij}) + P_2(\mathbf{u}_j \cdot \mathbf{s}_{ij})] + \mu \left[(\mathbf{u}_i \cdot \mathbf{s}_{ij})(\mathbf{u}_j \cdot \mathbf{s}_{ij})(\mathbf{u}_i \cdot \mathbf{u}_j) - \frac{1}{9} \right] \right. \\ \left. + P_2(\mathbf{u}_i \cdot \mathbf{u}_j) \{ \nu + \rho [P_2(\mathbf{u}_i \cdot \mathbf{s}_{ij}) + P_2(\mathbf{u}_j \cdot \mathbf{s}_{ij})] \} \right\}, \quad (3)$$

where $\varepsilon_{ij} = \varepsilon$, $\varepsilon > 0$ for i, j nearest neighbours and 0 otherwise, $\mathbf{s}_{ij} = \mathbf{r}_{ij}/|\mathbf{r}_{ij}|$, $\mathbf{r}_{ij} = \mathbf{r}_i - \mathbf{r}_j$, with $\mathbf{r}_i, \mathbf{r}_j$ the position vectors of the i -th and j -th lattice points; $\mathbf{u}_i, \mathbf{u}_k$ are unit vectors along the axis of the two particles (or "spins") and P_2 is a second rank Legendre polynomial. The parameters λ, μ, ν, ρ are defined in terms of the splay, twist and bend elastic constants K_{11}, K_{22}, K_{33} as

$$\lambda = \frac{1}{3} \Lambda (2K_{11} - 3K_{22} + K_{33}); \quad (4)$$

$$\mu = 3\Lambda (K_{22} - K_{11}); \quad (5)$$

$$\nu = \frac{1}{3} \Lambda (K_{11} - 3K_{22} - K_{33}); \quad (6)$$

$$\rho = \frac{1}{3} \Lambda (K_{11} - K_{33}), \quad (7)$$

with Λ a factor with dimensions of length. The spins represent a cluster of neighboring molecules whose short range order is assumed to be maintained through the temperature range examined³³. We notice that the pseudo-potential in Eq. 3 is a mesoscopic, rather than a truly molecular one, as shown by the fact that it contains elastic constants, and thus it is temperature dependent. The one constant approximation case, i.e. $\lambda = \mu = \rho = 0$, $\nu = -1$, formally reduces Eq. 3 to the well-known Lebwohl-Lasher (LL) potential which correctly reproduces the orientational order characteristics of a nematic- isotropic (NI) phase transition³³. This transition occurs, for the bulk LL, at a reduced temperature²⁷ $T^* \equiv kT/\varepsilon = 1.1232$. While in simulating bulk systems³³ periodic boundary conditions are employed in all three directions, in the present case we have a finite thickness film and boundaries in the vertical direction are implemented, as mentioned before, by considering additional layers of particles, kept fixed during the simulation, with suitable orientations chosen to mimic the desired surface alignment³³. Here we consider uniaxial nematic films with hybrid conditions, homeotropic at the top and various degrees of ordering

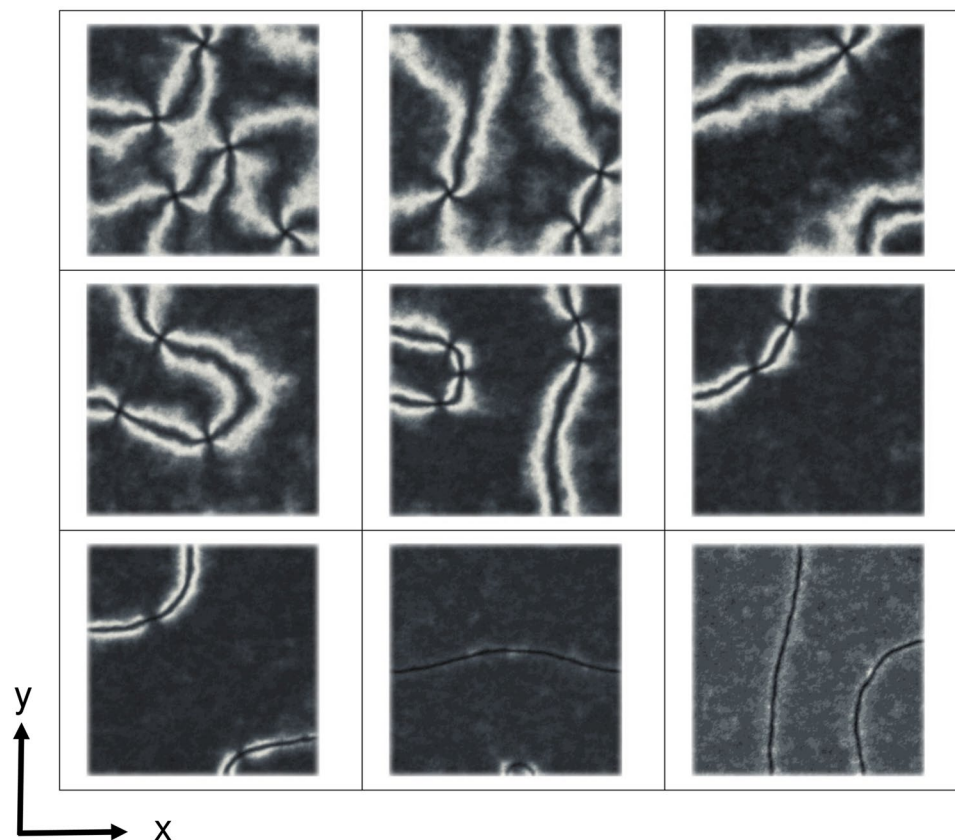


Figure 1. Optical images between crossed polars as obtained from a simulation of a $200 \times 200 \times (10 + 2)$ GHLR system with homeotropic alignment at $z = h$ and different surface ordering at the bottom ($z = 0$). The frames (from top left to bottom right) refer to a surface order parameter $\langle T_2 \rangle = 0.00$ (planar degenerate), 0.02, 0.05, 0.07, 0.10, 0.20, 0.30, 0.50 and 1.00 (perfect alignment along x). All have surface coupling $J = 0.5$ and elastic constants $K_{11} = 7.0$ pN, $K_2 = 4.4$ pN, $K_3 = 9.7$ pN.

at the bottom, from a random planar to a perfect alignment along the x direction. The starting configurations of the lattice were chosen to be completely aligned along the z direction and the evolution of the system was followed according to the classic Metropolis Monte Carlo procedure³⁴. The film was considered to be placed between crossed polarizers and polarizing microscope (POM) textures were simulated by means of a Müller matrix approach^{35–37}, assuming that the molecular domains represented by the spins act as birefringent retarders on the light propagating linearly across the film. In practice the following parameters were employed for computing the optical textures: film thickness $d = 5.3 \mu\text{m}$, ordinary and extraordinary refractive indices $n_o = 1.5$ and $n_e = 1.66$, and light wavelength $\lambda_0 = 545$ nm.

Simulation Results

We have considered a thin film of dimensions $200 \times 200 \times (h + 2)$, $h = 10$, system with the top and bottom boundary conditions implemented as described above. Empty (free) boundary conditions were employed instead at the other four lateral faces of the system. As we have shown in previous work²⁴ the value of J , the strength of coupling with the surface spins, can be related to the film thickness, in the sense that increasing the strength of the anchoring is somehow equivalent to simulating thinner films. In the present case we have chosen a coupling corresponding to $(1/2)$ of the molecular interaction strength, i.e. $J = 0.5$, value which is suitable to produce stable point defects for the hybrid nematic film with planar random orientation at the bottom. We have then considered various cases with increasing degree of surface ordering, $\langle T_2 \rangle$ at the bottom surface and the results are reported in Fig. 1. We see that, as $\langle T_2 \rangle$ increases, the point defects tend to lie on a line and that they then disappear forming a disclination line when the bottom surface spins are sufficiently aligned along x , with a (rough) critical threshold $\langle T_2 \rangle = 0.30$ – 0.40 for the present case, where we have used the elastic constants of 5CB, i.e. $K_{11} = 7.0$ pN, $K_2 = 4.4$ pN, $K_3 = 9.7$ pN.

To visualize nematic director field and defects, as shown in Fig. 2, we have followed Callan-Jones *et al.*^{3,38}, calculating the average ordering matrix $U_i = \langle \mathbf{u}_i \otimes \mathbf{u}_i \rangle$ at each lattice site i . The local director corresponds to the direction of the largest eigenvalue λ_1^i , while defects are identified from the so called Westin metric c_i^j , obtained taking the difference of the two largest eigenvalues: $c_i^j = \lambda_1^i - \lambda_2^i$ and noting that c_i^j tends to 1 for complete uniaxial order while it will tend to zero (or in practice have values below a given low threshold) at defects. We see that defects imprinted in the underlying partially disordered surface of the support are transmitted to the overlayer because of the rather strong surface anchoring imposed with the coupling parameter J . The effect of the ordering

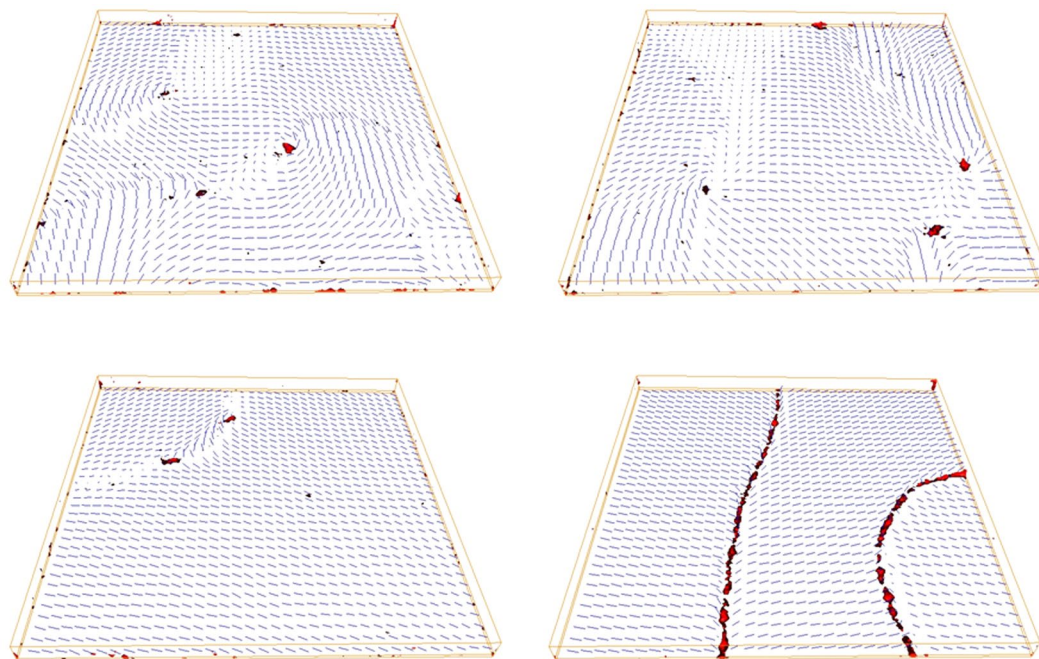


Figure 2. Plots of the local director at lattice sites and of the c_l Westin³⁸ metric isosurfaces corresponding to a defect (red) of the simulated sample for some of the cases presented in Fig. 1 with different values of ordering at the bottom surface ($z=0$). The frames refer to the first overlayer for a substrate with $\langle T_2 \rangle = 0.00$, i.e. planar random (top-left), 2% (top-right), 20% (bottom-left), and 100%, i.e. perfect alignment along x (bottom-right). The axes are the same as in Fig. 1.

along x at the bottom surface is evident when looking at the cases shown in Fig. 2. In Fig. 2 (top-left), which corresponds to a planar degenerate surface, two $+1$ and two -1 defects are visible, while in the other extreme of homogeneous in plane order Fig. 2 (bottom-right) the lack of imprinted orientations covering all the angular directions in the xy plane does not allow $+1$ and -1 defects and we see instead a line of $+\frac{1}{2}$ and of $-\frac{1}{2}$ defects in the family of xz plane cutting through the film. It is also apparent that the defects start at the lowest layers of the system and link the spin orientations induced by the bottom surface to the perfectly homeotropic alignment at the top (Fig. 3).

We notice that this scenario is due mainly to the specific type of boundary conditions and do not appear to depend on the different values of the elastic constants as can be verified by performing a simulation of a Lebwohl-Lasher model (which corresponds to the one elastic constant approximation) with the same surface order parameters (see Fig. 4). The effect of the difference in the elastic constants is to enhance the creation and stability of the point defects that continue to be present up to a large value of ordering at the bottom surface (see Fig. 1).

Experimental Approach

Optical experiments were performed to verify the behavior seen in simulations. A $6\ \mu\text{m}$ hybrid liquid crystal cell was prepared using a substrate with uniform homeotropic anchoring and one with planar anchoring with increasing degrees of uniaxial order. The substrate with homeotropic anchoring was prepared by spin coating a homeotropic aligning layer (JSR, JALS-2021-R2) on a glass substrate. The substrate with planar anchoring was prepared by spin-coating a photoaligning layer (DIC, LIA-03), and subsequently performing maskless photoalignment to create surfaces with orientational easy axis distributions with varying uniaxial order. Maskless photoalignment was performed using a home-built system comprising a LC display (LCD) projector, projection optics, and a rotating waveplate, PC-controlled, to sequentially project linearly polarized light at 1° increments (corresponding to 180 phase-levels) at predefined positions³⁹. The pixel resolution of the LCD projector was 1024×768 with a pixel size of approximately $1.5 \times 1.5\ \mu\text{m}^2$. The photoaligning layer was azobenzene-based, and chosen so as to set the orientational easy axis parallel to the substrate, in a direction perpendicular to the incident polarization. The wavelength of the patterning light was 436 nm.

Within one projection area, 9 regions with 278×178 pixels were prepared, each possessing different degrees of uniaxial order along the horizontal (x) direction. Three different sets of projections were made to create 25 regions covering $\langle T_2 \rangle$ values of 0.01 to 1.00. To realize a degree of bottom surface ordering corresponding, as far as possible, to that of the MC simulations, we have first randomly chosen the position of the desired percentage of pixels (or “spins” of the lattice model) where an alignment along x is then photoimprinted, and successively we have extracted from a uniform distribution the orientations at the remaining pixels so as to complete the pattern in each of the 25 regions. Between the various regions, a gap with uniaxial orientation along the y direction was

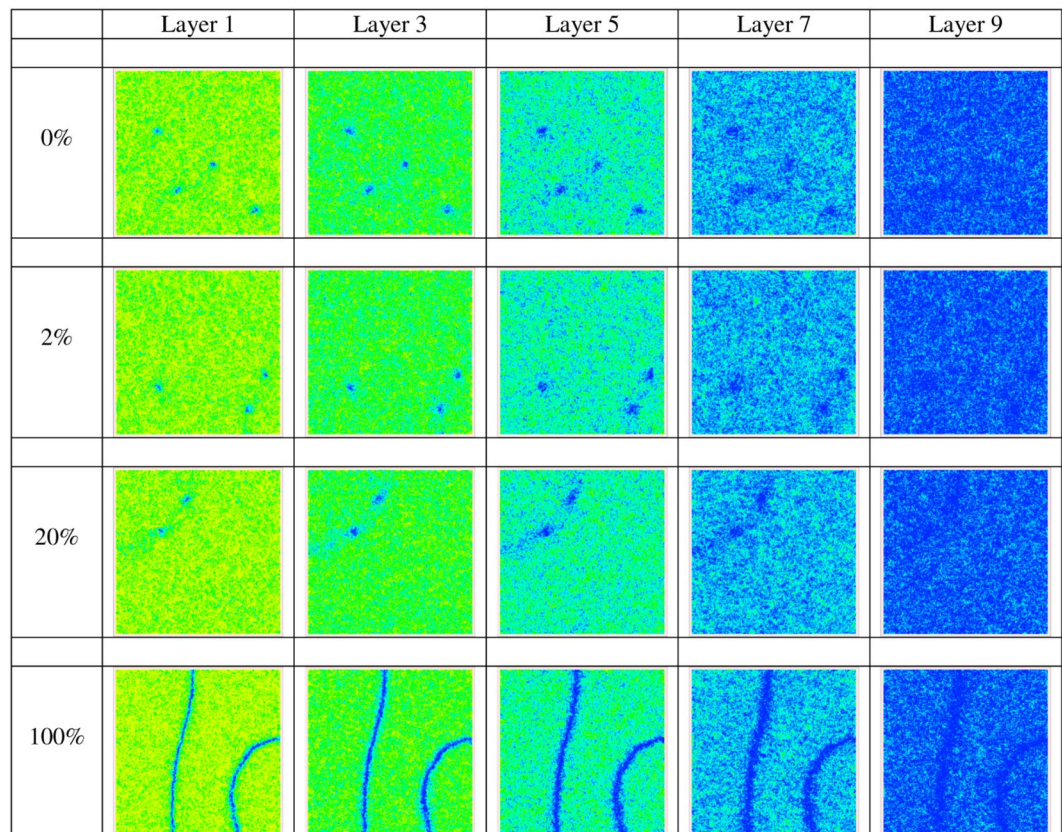


Figure 3. Snapshots of five layers of the nematic films starting from the bottom for four different percentages of ordering at the bottom surface of the film. Director field of the simulated samples for some values of ordering at the bottom surface corresponding to the cases presented in Fig. 2. The color of the spins varies from blue when they are oriented along z to yellow when they lie in the xy plane.

set. We notice that this arrangement, albeit similar, is not identical to the computer simulated one, where each region was treated independently from the others, thus avoiding by construction the possibility of cross-talk between the regions. The photoalignment pattern is shown in Fig. 5(a), where the degree of uniaxial order along the x horizontal direction increases from top-left to bottom right in each projected area. The region outside of the overall projection area was left untreated.

After cell preparation, a photopolymerizable nematic LC mixture, (RMM141C, Merck) was injected in the gap for observation of the optical texture by (POM, Nikon, LV100N POL). The reactive mesogen RMM141C was chosen because this LC showed a clear Schlieren texture on the photoalignment layer used, whereas other nematic LCs, for example the well-known 4-pentyl-4' cyanobiphenyl, showed the marble texture⁴⁰. The sample was heated to 70 °C, which is above the clearing point of the nematic ($T_{iso} \sim 67$ °C), and gradually cooled to 42 °C on a commercial hotplate (Instec, HCS622VXY-F4SYS). Because of the limited sample size, the defects tended to escape out of the patterned region after several 10 minutes; by photopolymerizing the texture after confirming that different textures appeared in the patterned regions.

Results and Discussions

Figure 5(b) shows POM images of the sample observed between crossed polarizers. One can recognize the 25 photoaligned regions, showing different optical textures depending on the value of $\langle T_2 \rangle$. In the regions with low uniaxial order, a schlieren texture is observed, which cannot be distinguished from that observed in the region without the patterning. However, as the uniaxial surface order is increased, the region gradually becomes darker, and shows string-like textures. The difference is apparent also when the analyzer is removed (Fig. 5(c)); in regions with low uniaxial order, isolated point defects are visible, whereas in high-order regions, an apparent line defect is observed. Figure 6 shows magnified images of regions with $\langle T_2 \rangle = 0.01, 0.45,$ and 1.0 to enhance the change in the optical textures as the bottom ordering increases.

The first general observation is that there is at least a qualitative agreement between simulations and real experiments. In simulations (for the LL model, Fig. 4, corresponding to the one elastic constant approximation), a transition occurs from the standard schlieren texture (dark brushes in a bright background) to a more line-like texture at approximately $\langle T_2 \rangle \sim 0.07$ – 0.1 , where two of the four dark brushes emanating from a point defect become elongated and surrounded by two narrow bright bands. This transition is observed at $\langle T_2 \rangle \sim 0.1$ in experiment, which is a satisfactory agreement considering that the simulations deal with an idealized liquid crystal

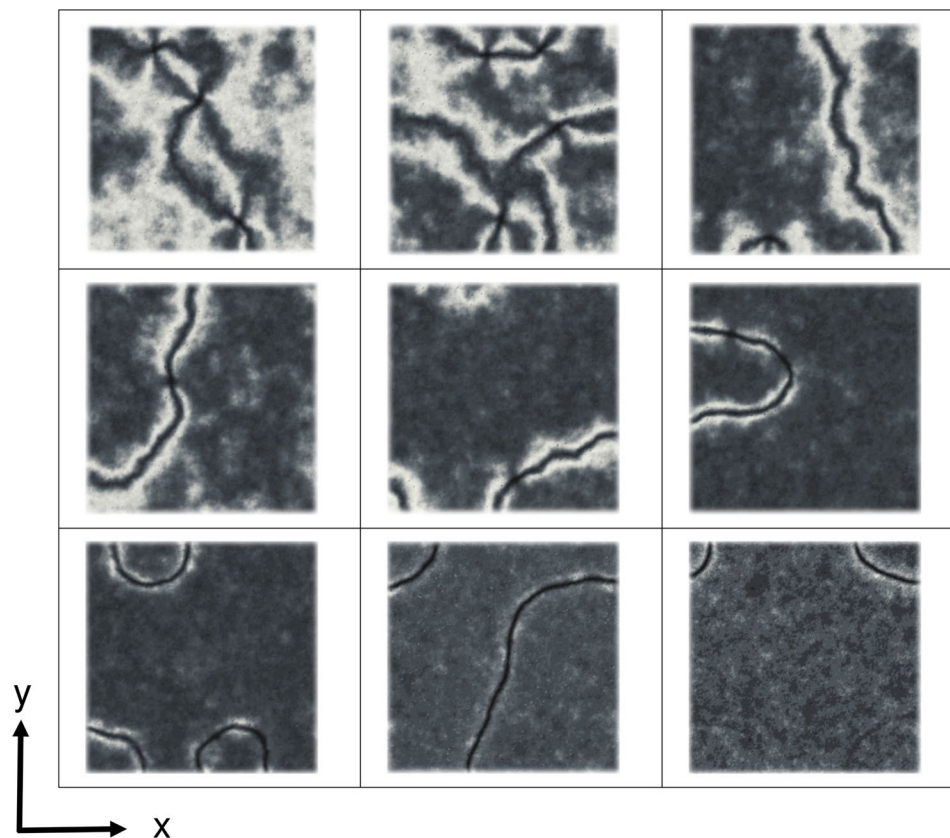


Figure 4. Polarized optical images as obtained from a simulation of a $200 \times 200 \times (10 + 2)$ Lebwohl-Lasher system where the three elastic constants are equal. The geometry of the system is the same as for the Gruhn-Hess case and the ordering at the bottom surface, $\langle T_2 \rangle$, is (from top left to bottom right): 0 (planar random), 0.02, 0.05, 0.07, 0.10, 0.20, 0.30, 0.50 and 1.00 (perfect alignment along x). The coupling with the surfaces was chosen to be $J = 0.5$.

and no attempt has been made to fit the parameters of the actual material used in experiments. For the case of different elastic constants the transition appears to move to different values of $\langle T_2 \rangle$, see for example Fig. 1, but the main features of the behaviour do not change.

With an increase in surface order, the width of the bright bands becomes narrower, in both simulations and experiments. However, simulations show a near-complete suppression of light leakage at $\langle T_2 \rangle > 0.5$, whereas in experiment the bright bands remain. We attribute this difference to the fact that point defects were observed in experiment in all regions including $\langle T_2 \rangle = 1.0$, whereas simulations gave none in this limit. Detection of the defect strength by rotating the sample indicated that defects have strengths of either $+1$ or -1 , and the optical texture (both schlieren and line-like) occurs as to connect oppositely charged defects. Figure 5(d) shows a POM image of the sample taken after inserting a first order retardation plate ($\Delta = 530$ nm) in the optical path, demonstrating the alternation in the azimuthal tilt direction in each segment of the line-like texture. Point defects impose topological boundary conditions such that the director must rotate in a specific direction around the defect core, and in addition, since oppositely charged defects are connected, a π rotation in the director must occur along the normal of a line that connects two point defects (Fig. 7). Since this topological constraint requires some regions to be aligned in directions not parallel to the polarizers, light leakage must occur.

It is very difficult to compare the anchoring strength which results from the complex fabrication process described in experiment and that employed in the simulations, which is probably significantly higher than that in experiment. If this is the case, as we believe, this factor strongly disfavors the deformations associated with point defects in the simulated textures. Also, since the nematic phase is experimentally obtained by cooling from the random isotropic phase, the point defects formed at the phase transition may have entered a metastable state and remained as a singularity. Furthermore we have boundary conditions in the $x - y$ plane, i.e. at the four sides of the sample cell, that are “empty” in the case of the MC simulations, while in the real samples we have narrow oriented frames that are part of an overall, somehow connected surface area, as shown by the continuity of the patterns between neighbouring cells in Fig. 5(b). Given all these possible sources of discrepancy it is comforting to observe that the textures and their change upon increasing the surface order are quite similar, and we take this as a validation of the computational results. This being the case, we can then use the ability of simulations to examine the director field and its defects across the film thickness, adding a visualization capability in three dimensions that complements the xy projections observed from POM. For instance, we see from Fig. 2 at a 2%

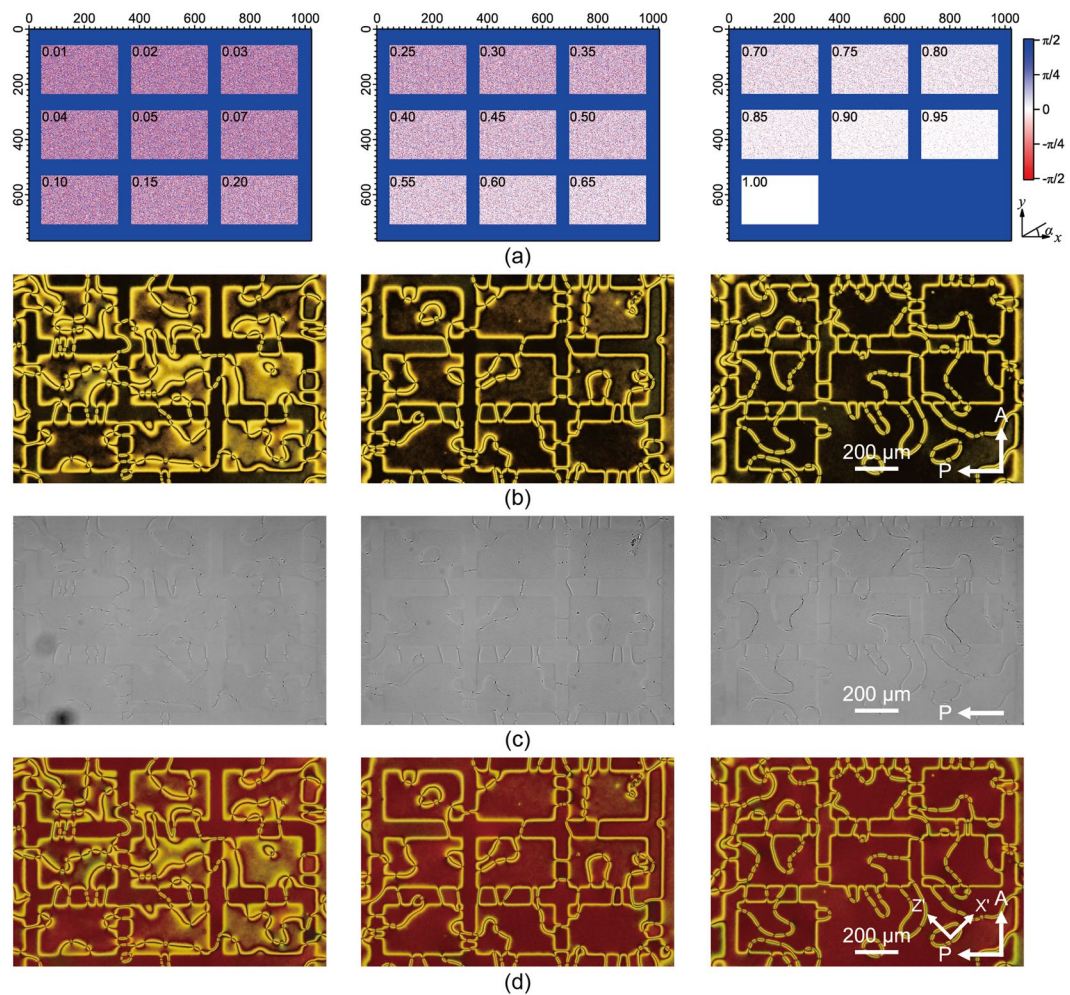


Figure 5. (a) Design of the easy axis distribution created in experiment, where the values written in each of the 25 regions indicate the designated $\langle T_z \rangle$ values. (b) Experimental POM images of the prepared hybrid cell. (c) Optical Microscopy images with the analyzer removed. Images have been converted to greyscale and the brightness and contrast were adjusted using Adobe Photoshop (using the same parameters for the three images) to enhance the difference in the defect textures. (d) POM images with a first order retardation plate ($\Delta = 530 \text{ nm}$).

planar order (top right) that the line feature actually connects opposite sign point defects, as found in experiment. Simulations also indicate that the defect region is in all cases adjacent to the bottom partially ordered surface and that the defects appear as vertical escaped walls rather than as disclination lines, as they appear from the inevitably two dimensional projection offered by POM. We notice, however, that the fact that the defects originate close to the planar anchoring surface appears to be at variance with respect to the results of ref. ²⁸, where disclinations lines are observed in a hybrid cell but the disclination lines appear to be located in the middle of the sample. On the other hand this could be due to pinning at the silica microspheres used as spacers, as stated in²⁸, which are not present in our case neither in the simulations nor, as mentioned before, in the experiment. We believe that the curvature of the spheres, necessarily non-negligible across the sample thickness and the anchoring of orientation at their silica surface, which is not specified and should depend on their pre-treatment could provide significantly different boundary conditions.

Conclusions

In the present study we have investigated, by a combination of Monte Carlo simulations and real experiments, a hybrid cell where one (the top one in our case) of the two facing surfaces is always inducing homeotropic alignment, while the other has an in plane ordering varying from fully random to perfectly homogeneous. We have found, that a random, degenerate, anchoring favors point defects, while homogeneous alignment favors the appearance of filament like defects. Tuning the in plane order of the bottom surface to values intermediate between the two extremes allows to follow the change over from one type of defect to the other. In particular, performing simulations with anisotropic and isotropic elastic constants, we have observed that the transition is mainly due to the surface alignment rather than on the details of the nematic elastic constants. Examining snapshots of the film layer by layer (Fig. 3) it appears that the transitions from planar to vertical alignment is a sudden

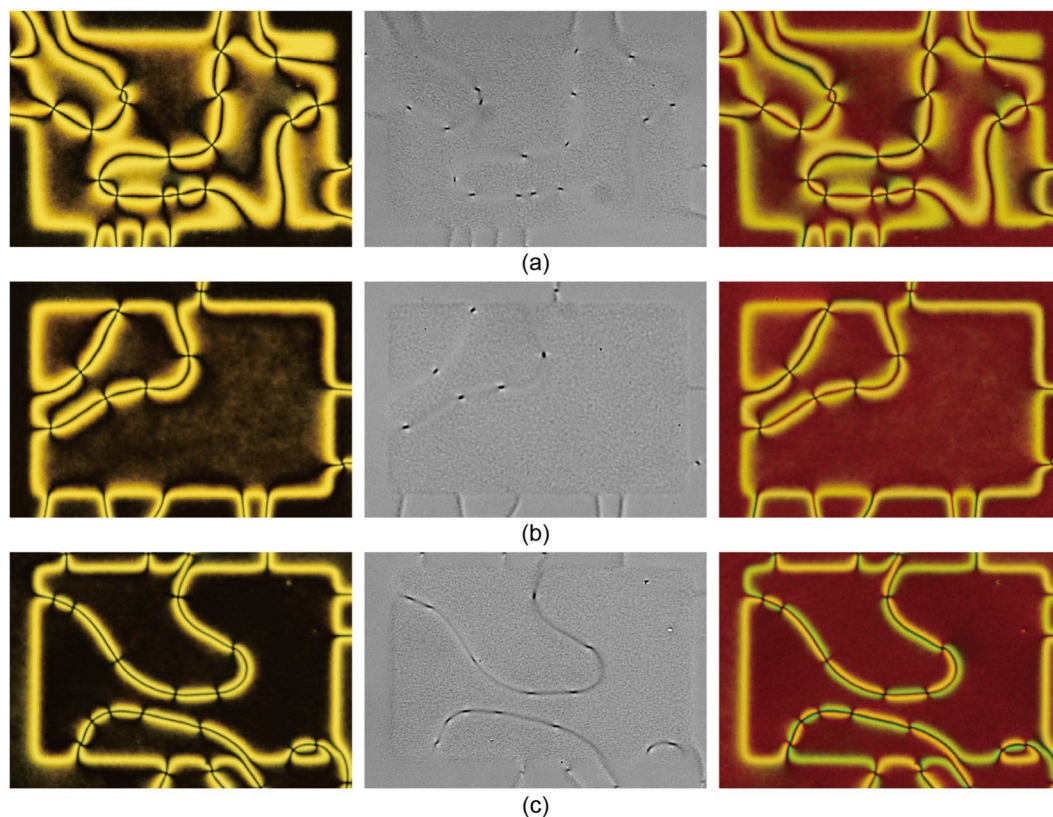


Figure 6. Magnified images of regions with (a) $\langle T_2 \rangle = 0.01$, (b) 0.45, and (c) 1.0. The orientations of the polarizers and the waveplate are the same as Fig. 5.

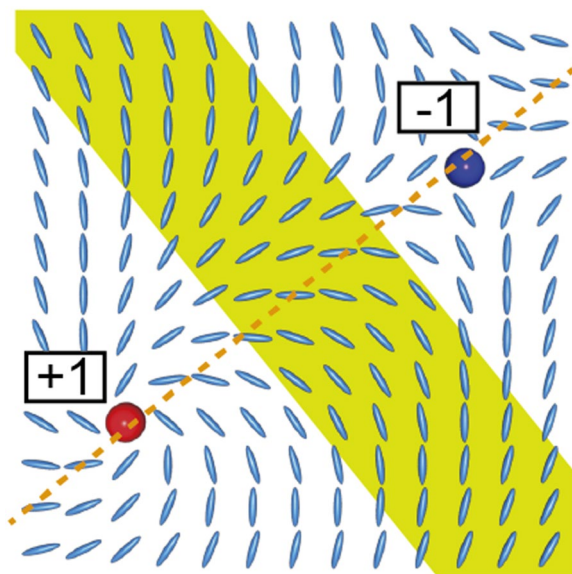


Figure 7. Topological requirement of π director rotation (yellow stripe) between two oppositely charged point defects.

one, starting from the bottom overlayer, rather than from an intermediate one. We believe that this finding is an example of a major innovation of the present work: the combined use of Monte Carlo simulations and optical experiments. On one hand the 2D polarized microscopy textures obtained from experiment can validate the MC simulations. On the other, the simulations, once validated, allow a detailed visualization of the 3D molecular organization across the film, complementing the 2D projections produced by POM experiments and offering an important way of discriminating between models.

Received: 30 April 2019; Accepted: 11 September 2019;

Published online: 29 November 2019

References

- Kleman, M. *Points, Lines and Walls: In Liquid Crystals, Magnetic Systems and Various Ordered Media* (Wiley, New York, 1982).
- Nelson, D. R. Toward a tetravalent chemistry of colloids. *Nano Lett.* **2**, 1125–1129 (2002).
- Skačej, G. & Zannoni, C. Controlling surface defect valence in colloids. *Phys. Rev. Lett.* **100**, 197802 (2008).
- Lavrentovich, O. D. Liquid crystals, photonic crystals, metamaterials, and transformation optics. *PNAS* **108**, 5143–5144 (2011).
- Tkalec, U., Ravnik, M., Copar, S., Zumer, S. & Musevic, I. Reconfigurable knots and links in chiral nematic colloids. *Science* **333**, 62–65, <https://doi.org/10.1126/science.1205705> (2011).
- Alexander, G. P., Chen, B. G. G., Matsumoto, E. A. & Kamien, R. D. Colloquium: Disclination loops, point defects, and all that in nematic liquid crystals. *Rev. Mod. Phys.* **84**, 497–514 (2012).
- Liang, H.-L., Zentel, R., Rudquist, P. & Lagerwall, J. Towards tunable defect arrangements in smectic liquid crystal shells utilizing the nematic–smectic transition in hybrid-aligned geometries. *Soft Matter* **8**, 5443 (2012).
- Pelliser, L., Coursault, D. & Lacaze, E. Formation of nanoparticle chains within liquid crystal defect arrays. In Fesenko, O., Yatsenko, L. & Brodin, M. (eds) *Nanomaterials Imaging Techniques, Surface Studies, and Applications*, vol. 146 of *Springer Proceedings in Physics*, 51–59 (2013).
- Tasinkevych, M., Campbell, M. G. & Smalyukh, I. Splitting, linking, knotting, and solitonic escape of topological defects in nematic drops with handles. *Proc. Natl. Acad. Sci. United States Am.* **111**, 16268–16273, <https://doi.org/10.1073/pnas.1405928111> (2014).
- Gharbi, M. A., Nobili, M. & Blanc, C. Use of topological defects as templates to direct assembly of colloidal particles at nematic interfaces. *J. Colloid Interface Sci.* **417**, 250–255 (2014).
- Coursault, D. *et al.* Self-organized arrays of dislocations in thin smectic liquid crystal films. *Soft Matter* **12**, 678–688 (2016).
- Gharbi, M. A. *et al.* Smectic gardening on curved landscapes. *Langmuir* **31**, 11135–11142 (2015).
- Lee, E. *et al.* Fine golden rings: tunable surface plasmon resonance from assembled nanorods in topological defects of liquid crystals. *Adv. Mater.* **28**, 2731–2736 (2016).
- Yoshida, H., Asakura, K., Fukuda, J. & Ozaki, M. Three-dimensional positioning and control of colloidal objects utilizing engineered liquid crystalline defect networks. *Nat. Commun.* **6**, <https://doi.org/10.1038/ncomms8180> (2015).
- Luo, Y. M., Serra, F. & Stebe, K. J. Experimental realization of the "lock-and-key" mechanism in liquid crystals. *Soft Matter* **12**, 6027–6032 (2016).
- Peng, C. H., Turiv, T., Guo, Y. B., Wei, Q. H. & Lavrentovich, O. D. Command of active matter by topological defects and patterns. *Science* **354**, 882–885 (2016).
- Kleman, M. & Lavrentovich, O. D. *Soft Matter Physics* (Springer, Berlin, 2003).
- Kleman, M. & Lavrentovich, O. D. Topological point defects in nematic liquid crystals. *Philos. Mag.* **86**, 4117–4137 (2006).
- Bates, M. A., Skačej, G. & Zannoni, C. Defects and ordering in nematic coatings on uniaxial and biaxial colloids. *Soft Matter* **6**, 655–663 (2010).
- Mermin, N. D. The topological theory of defects in ordered media. *Rev. Mod. Phys.* **51**, 591–648 (1979).
- Afghah, S., Selinger, R. L. B. & Selinger, J. V. Visualising the crossover between 3d and 2d topological defects in nematic liquid crystals. *Liq. Cryst.* 1–11, <https://doi.org/10.1080/02678292.2018.1494857> (2018).
- Ohzono, T. *et al.* Uncovering different states of topological defects in schlieren textures of a nematic liquid crystal. *Sci. Reports* **7**, <https://doi.org/10.1038/s41598-017-16967-1> (2017).
- Cladis, P. E. & Kleman, M. Non-singular disclinations of strength $s = +1$ in nematics. *J. De Physique* **33**, 591 (1972).
- Chiccoli, C., Lavrentovich, O. D., Pasini, P. & Zannoni, C. Monte Carlo simulations of stable point defects in hybrid nematic films. *Phys. Rev. Lett.* **79**, 4401–4404 (1997).
- Lavrentovich, O. D. & Pergamenschik, V. M. Patterns in thin liquid-crystal films and the divergence (surfacelike) elasticity. *Int. J. Mod. Phys. B* **9**, 2389–2437 (1995).
- Lebwohl, P. A. & Lasher, G. Nematic liquid crystal order: a Monte Carlo calculation. *Phys. Rev. A* **6**, 426–429 (1972).
- Fabbri, U. & Zannoni, C. A Monte Carlo investigation of the Lebwohl-Lasher lattice model in the vicinity of its orientational phase-transition. *Mol. Phys.* **58**, 763–788 (1986).
- Buscaglia, M., Lombardo, G., Cavalli, L., Barberi, R. & Bellini, T. Elastic anisotropy at a glance: the optical signature of disclination lines. *Soft Matter* **6**, 5434–5442 (2010).
- Denham, J. Y., Luckhurst, G. R., Zannoni, C. & Lewis, J. W. Computer-simulation studies of anisotropic systems 0.3. Two-dimensional nematic liquid-crystals. *Mol. Cryst. Liq. Cryst.* **60**, 185–205 (1980).
- Gruhn, T. & Hess, S. Monte Carlo simulation of the director field of a nematic liquid crystal with three elastic coefficients. *Z. Naturforsch., A: Phys. Sci.* **51**, 1–9 (1996).
- Romano, S. Elastic constants and pair potentials for nematogenic lattice models. *Int. J. Mod. Phys. B* **12**, 2305–2323 (1998).
- Luckhurst, G. R. & Romano, S. Computer simulation study of a nematogenic lattice model based on an elastic energy mapping of the pair potential. *Liq. Cryst.* **26**, 871–884 (1999).
- Pasini, P. & Zannoni, C. *Advances in the Computer Simulations of Liquid Crystals* (Kluwer, Dordrecht, 2000).
- Landau, D. P. & Binder, K. *A Guide to Monte Carlo Simulations in Statistical Physics* (Cambridge University Press, Cambridge, 2000).
- Kilian, A. Computer simulations of nematic droplets. *Liq. Cryst.* **14**, 1189–1198 (1993).
- Ondris-Crawford, R. *et al.* Microscope textures of nematic droplets in polymer dispersed liquid-crystals. *J. Appl. Phys.* **69**, 6380–6386 (1991).
- Berggren, E., Zannoni, C., Chiccoli, C., Pasini, P. & Semeria, F. Computer simulations of nematic droplets with bipolar boundary-conditions. *Phys. Rev. E* **50**, 2929–2939 (1994).
- Callan-Jones, A. C. *et al.* Simulation and visualization of topological defects in nematic liquid crystals. *Phys. Rev. E* **74**, 061701 (2006).
- Kobashi, J., Yoshida, H. & Ozaki, M. Planar optics with patterned chiral liquid crystals. *Nat. Photonics* **10**, 389–392 (2016).
- Dierking, I. *Textures of Liquid Crystals* (Wiley, NY, 2003).

Acknowledgements

This research was supported by JST, PRESTO Grant Number JPMJPR151D, Japan and INFN-Bologna Section. We thank O.D. Lavrentovich and F. Serra for useful discussions in the preliminary stages of this work. C.Z. would like to thank the Isaac Newton Institute for Mathematical Sciences for support and hospitality during the programme “Mathematical Design of New Materials” when work on this paper was completed. This was supported by EPSRC Grant Number EP/R014604/1.

Author contributions

C.C., P.P., G.S. and C.Z. conceived and conducted the simulations and analyzed the simulations results. H.Y., T.H., K.S., T.O. and M.O. performed the experiments and analyzed the results. All authors reviewed the manuscript.

Competing interests

The authors declare no competing interests.

Additional information

Correspondence and requests for materials should be addressed to C.Z.

Reprints and permissions information is available at www.nature.com/reprints.

Publisher's note Springer Nature remains neutral with regard to jurisdictional claims in published maps and institutional affiliations.



Open Access This article is licensed under a Creative Commons Attribution 4.0 International License, which permits use, sharing, adaptation, distribution and reproduction in any medium or format, as long as you give appropriate credit to the original author(s) and the source, provide a link to the Creative Commons license, and indicate if changes were made. The images or other third party material in this article are included in the article's Creative Commons license, unless indicated otherwise in a credit line to the material. If material is not included in the article's Creative Commons license and your intended use is not permitted by statutory regulation or exceeds the permitted use, you will need to obtain permission directly from the copyright holder. To view a copy of this license, visit <http://creativecommons.org/licenses/by/4.0/>.

© The Author(s) 2019